

DRAFT

CMS Paper

The content of this note is intended for CMS internal use and distribution only

2024/10/29

Archive Hash: 32611a6

Archive Date: 2023/09/28

Search for Dark Matter Produced in Association with a Resonant Bottom-Quark Pair in Proton-Proton Collisions at $\sqrt{s} = 13 \text{ TeV}$

The CMS Collaboration

Abstract

A search for dark matter (DM) produced in association with a resonant $b\bar{b}$ pair is performed in proton-proton collisions at a center-of-mass energy of 13 TeV collected with the CMS detector during the Run 2 of the Large Hadron Collider. The analyzed data sample corresponds to an integrated luminosity of 137 fb^{-1} . Results are interpreted in terms of a novel theoretical model of DM production at the LHC that predicts the presence of a Higgs-boson-like particle in the dark sector, motivated simultaneously by the need to generate the masses of the particles in the dark sector and the possibility to relax constraints from the DM relic abundance by opening up a new annihilation channel. If such a dark Higgs boson decays into standard model (SM) states via a small mixing with the SM Higgs boson, one obtains characteristic large-radius jets in association with missing transverse momentum that can be used to efficiently discriminate signal from backgrounds. Limits on the signal strength of different dark Higgs boson mass hypotheses below 160 GeV are set for the first time with CMS data.

This box is only visible in draft mode. Please make sure the values below make sense.

PDFAuthor:	M. Cremonesi, A. Das, M. Donega, S. Eisenberger, E. Ertorer, A. Hall, M. Hildreth, B. Jayatilaka, J. Lee, N. Macilla, M. Marchegiani, C.-S. Moon, I. Pedraza, N. Smith, T. Tomei, D. Valsecchi, R. Wallny, M. Wassmer1, Z. Ye
PDFTitle:	Search for Dark Matter Produced in Association with a Resonant Bottom-Quark Pair
PDFSubject:	CMS
PDFKeywords:	CMS, physics, software, computing

Please also verify that the abstract does not use any user defined symbols

1 It is well established from astrophysical observations that most of the matter in the Universe is
 2 comprised of dark matter (DM) [1]. However, its particle nature remains unknown and cannot
 3 be accommodated within the standard model (SM). One of the leading hypotheses is that DM is
 4 composed of stable, electrically neutral, massive particles which interact with baryons at least
 5 via the gravitational force. If such a DM particle also interacts non-gravitationally with SM
 6 particles, then DM could be produced in proton-proton collisions at the Large Hadron Collider
 7 (LHC) at CERN.
 8 Since DM particles, once produced, do not leave any detectable signal in the detector, they
 9 cannot be directly observed. However, their presence can be inferred if they are produced in
 10 association with a visible SM particle X. Such processes generate final states commonly referred
 11 to as mono-X or $p_T^{\text{miss}} + X$ signatures, where p_T^{miss} is the missing transverse momentum [2].
 12 Typically, the most sensitive analysis channel to DM production is the one that searches for
 13 DM produced in association with a gluon or a quark emitted as initial state radiation (ISR),
 14 known as the mono-jet channel.
 15 The mono-jet DM searches at the LHC [3, 4] have strongly constrained the parameter space
 16 in which DM particles can obtain their relic abundance from direct annihilation into SM final
 17 states. This tension is relaxed if DM particles are not the lightest state in the dark sector, lead-
 18 ing to new annihilation channels. If the DM mass is generated via a Higgs mechanism in the
 19 dark sector and the resulting dark Higgs boson is lighter than DM, a new annihilation channel
 20 where DM particles annihilate into a pair of dark Higgs bosons (h_s), with subsequent decay
 21 into SM states, would be possible. This would easily set the observed relic abundance. Assum-
 22 ing a small mixing with the SM Higgs boson, a light dark Higgs boson decays with the same
 23 branching fraction of the SM Higgs boson, which vary depending on its mass. If the dark sector
 24 includes an additional spin-1 Z' mediator, then the probability of the Z' boson being produced
 25 and radiating a dark Higgs boson (dark-Higgsstrahlung) can be large [5]. A representative
 26 Feynman diagram for this signal model is shown in Fig. 1.
 27 Searches for dark Higgs boson production in association with DM particles have already been
 28 performed by the ATLAS [6] and the CMS [7] Collaborations. These searches focus on heavier
 29 dark Higgs boson mass hypotheses, larger than 160 GeV. For dark Higgs bosons of such mass
 30 the decay into a pair of W boson is the dominant one. In this paper, we present the search for
 31 the associated production of DM and a light dark Higgs boson (with mass less than 160 GeV),
 32 which decays predominantly into a pair of b quarks, performed for the first time at the LHC.
 33 This final state results in a distinctive signature of large missing transverse momentum, arising
 34 from the decay of the Z' mediator into DM, and a highly-boosted large-radius jet, originated
 35 by the hadronization of two b quarks from the dark Higgs boson decay. Results are presented
 36 for the full dataset of 137.2 fb^{-1} collected by the CMS experiment at a center-of-mass energy of
 37 13 TeV during Run 2 of the LHC.

38 **1 The CMS detector and event reconstruction**

39 The central feature of the CMS apparatus is a superconducting solenoid of 6 m internal diame-
 40 ter, providing a magnetic field of 3.8 T. Within the solenoid volume are a silicon pixel and strip
 41 tracker, a lead tungstate crystal electromagnetic calorimeter (ECAL), and a brass and scintilla-
 42 tor hadron calorimeter (HCAL), each composed of a barrel and two endcap sections. Forward
 43 calorimeters extend the pseudorapidity (η) coverage provided by the barrel and endcap detec-
 44 tors. Muons are detected in gas-ionization detectors embedded in the steel flux-return yoke
 45 outside the solenoid.

46 The silicon tracker measures charged particles within the pseudorapidity range $|\eta| < 2.5$. During
 47 the LHC running period when the data used in this paper were recorded, the silicon tracker
 48 consisted of 1856 silicon pixel and 15 148 silicon strip detector modules.

49 In the region $|\eta| < 1.74$, the HCAL cells have widths of 0.087 in pseudorapidity and 0.087
 50 in azimuth (ϕ). In the η - ϕ plane, and for $|\eta| < 1.48$, the HCAL cells map on to 5×5 arrays
 51 of ECAL crystals to form calorimeter towers projecting radially outwards from close to the
 52 nominal interaction point. For $|\eta| > 1.74$, the coverage of the towers increases progressively
 53 to a maximum of 0.174 in $\Delta\eta$ and $\Delta\phi$. The hadron forward (HF) calorimeter uses steel as an
 54 absorber and quartz fibers as the sensitive material. The two halves of the HF are located 11.2 m
 55 from the interaction region, one on each end, and together they provide coverage in the range
 56 $3.0 < |\eta| < 5.2$.

57 Events of interest are selected using a two-tiered trigger system. The first level (L1), composed
 58 of custom hardware processors, uses information from the calorimeters and muon detectors to
 59 select events at a rate of around 100 kHz within a fixed latency of about $4 \mu\text{s}$ [8]. The second
 60 level, known as the high-level trigger (HLT), consists of a farm of processors running a version
 61 of the full event reconstruction software optimized for fast processing, and reduces the event
 62 rate to around 1 kHz before data storage [9].

63 A more detailed description of the CMS detector, together with a definition of the coordinate
 64 system used and the relevant kinematic variables, can be found in Ref. [10].

65 The candidate vertex with the largest value of summed physics-object transverse momenta p_T^2
 66 is taken to be the primary vertex (PV) of the pp interaction. The physics objects are the jets,
 67 clustered using the jet finding algorithm [11, 12] with the tracks assigned to candidate vertices
 68 as inputs, and the associated p_T^{miss} , taken as the negative vector sum of the p_T of those jets.

69 A particle-flow (PF) algorithm [13] aims to reconstruct and identify each individual particle in
 70 an event, with an optimized combination of information from the various elements of the CMS
 71 detector. In this process, the identification of the PF candidate type (photon, electron, muon,
 72 and charged and neutral hadrons) plays an important role in the determination of the particle
 73 direction and energy. The energy of photons is obtained from the ECAL measurement. The
 74 energy of electrons is determined from a combination of the electron momentum at the PV as
 75 determined by the tracker, the energy of the corresponding ECAL cluster, and the energy sum
 76 of all bremsstrahlung photons spatially compatible with originating from the electron track.
 77 The energy of muons is obtained from the curvature of the corresponding track. The energy of
 78 charged hadrons is determined from a combination of their momentum measured in the tracker
 79 and the matching ECAL and HCAL energy deposits, corrected for the response function of the
 80 calorimeters to hadronic showers. Finally, the energy of neutral hadrons is obtained from the
 81 corresponding corrected ECAL and HCAL energies.

82 The missing transverse momentum vector \vec{p}_T^{miss} is computed as the negative vector sum of
 83 the transverse momenta of all the PF candidates in an event, and its magnitude is denoted as
 84 p_T^{miss} . The \vec{p}_T^{miss} is modified to account for corrections to the energy scale and resolution of
 85 the reconstructed jets in the event [14]. Anomalous high- p_T^{miss} events can be due to a variety
 86 of reconstruction failures, detector malfunctions, or noncollision backgrounds. Such events
 87 are rejected by dedicated filters that are designed to eliminate more than 85–90% of the spuri-
 88 ous high- p_T^{miss} events with a signal efficiency exceeding 99.9% [14]. For each event, hadronic
 89 jets are clustered from the PF candidates using the infrared- and collinear-safe anti- k_T algo-
 90 rithm [11, 12] with a distance parameter of 0.4 or 1.5. Depending on the respective distance
 91 parameter, these jets are referred to as “AK4” or “AK15” jets. Jet momentum is determined

as the vectorial sum of all particle momenta in the jet, and is found from simulation to be, on average, within 5 to 10% of the true momentum over the entire p_T spectrum and detector acceptance [15]. Additional pp interactions within the same or nearby bunch crossings (pileup) can contribute additional tracks and calorimetric energy depositions to the jet momentum. To mitigate this effect, charged particles identified as not originating from the PV are discarded and an offset correction is applied to correct for the remaining neutral pileup contributions [15]. Jet energy corrections are derived from simulation to bring the measured response of jets to that of particle-level jets on average. In situ measurements of the momentum balance in the dijet, $\gamma + \text{jet}$, $Z + \text{jet}$, and multijet events are used to account for any residual differences in the jet energy scale (JES) and jet energy resolution (JER) in data and simulation [15]. The jet energy resolution amounts typically to 15–20% at 30 GeV, 10% at 100 GeV, and 5% at 1 TeV [15]. Additional selection criteria [16] are applied to each jet to remove jets potentially dominated by anomalous contributions from various subdetector components or reconstruction failures. Narrow AK4 jets are also required to pass quality criteria based on the composition of the jet in terms of different types of PF candidates, such as a minimum charged-hadron energy fraction of 10% and a maximum neutral-hadron energy fraction of 80% [16].

Large-radius AK15 jets are used for the identification of the decays of the dark Higgs boson into a b-quark pair. The pileup-per-particle identification (PUPPI) algorithm [17] is used to mitigate the effect of pileup at the reconstructed-particle level, making use of local shape information, event pileup properties, and tracking information. Charged particles identified as not originating from the PV are discarded. For each neutral particle, a local shape variable is computed using the surrounding charged particles within the tracker acceptance ($|\eta| < 2.5$) compatible with the PV, and using both charged and neutral particles in the region outside of the tracker coverage. The momenta of the neutral particles are then rescaled according to their probability to originate from the PV deduced from the local shape variable, avoiding the need for jet-based pileup corrections [16]. The modified mass drop tagger algorithm [18, 19], also known as the soft-drop (SD) algorithm, with the angular exponent $\beta = 0$, soft cutoff threshold $z_{\text{cut}} < 0.1$, and characteristic radius $R_0 = 1.5$ [20], is applied to remove soft, wide-angle radiation from the jet.

2 Simulated samples

Monte Carlo (MC) simulated event samples are used to model signal and background contributions to all the analysis regions. In all cases, parton showering, hadronization, and underlying event properties are modeled using PYTHIA [21] version 8.202 or later with the underlying event tune CUETP8M1 or CP5 [22], based on the year of data taking. Simulation of interactions between particles and the CMS detector is based on GEANT4 [23]. The NNPDF 3.0 next-to-next-to-leading order (NNLO) [24] and the NNPDF 3.1 NNLO [25] parton distribution functions (PDFs) are used for the generation of all samples based on the year of data taking. The same reconstruction algorithms used for data are applied to simulated samples.

For the V + jets processes, predictions with up to two partons in the final state are obtained at leading order (LO) in QCD using MADGRAPH5_aMC@NLO [26] with the MLM matching scheme [27] between the jets from the matrix element calculations and the parton shower. Samples of events with top quark pairs are generated at next-to-leading (NLO) in QCD with up to two additional partons in the matrix element calculations using MADGRAPH5_aMC@NLO and the FxFx jet matching scheme [28]. Their cross sections are normalized to the inclusive cross section of the top quark pair production at NNLO in QCD [29]. Events with single top quarks are simulated using POWHEG 2.0 [30, 31] and normalized to the inclusive cross section calculated at NLO in QCD [32, 33]. Production of diboson events (WW, WZ, and ZZ) is simulated

138 at NLO in QCD using PYTHIA, and normalized to the cross sections at NNLO precision for
 139 WW production [34] and at NLO precision for the others [35]. Several production mechanisms
 140 of the SM Higgs boson decaying into a bottom-quark pair are also produced at LO with the
 141 POWHEG generator. Samples of QCD multijet production events are generated at LO using
 142 MADGRAPH5_aMC@NLO.

143 The MC samples for the dark Higgs boson signal process are generated with the MADGRAPH5_aMC@NLO
 144 with up to one additional parton in the matrix element calculations at LO with the MLM match-
 145 ing scheme. The values of the vector coupling g_q between the Z' mediator and the quarks, as
 146 well as the axial coupling g_χ between the mediator and DM particles, are set to $g_q = 0.25$ and
 147 $g_\chi = 1.0$, respectively, as recommended by the LHC Dark Matter Working Group [36]. Separate
 148 samples are generated for different mass hypotheses for the mediator, DM particles, and dark
 149 Higgs boson.

150 3 Event selection

151 The key feature of the analysis is the extensive use of control data samples for the purpose of
 152 precise prediction of the background contributions in the signal regions (SRs), which contain
 153 events with a large-radius, high- p_T jet and large p_T^{miss} . The leading SM background contribu-
 154 tions originate from $Z \rightarrow \nu\nu$ and $W \rightarrow \ell\nu$ production ($\ell = e, \mu, \tau$), the properties of which
 155 are constrained using control regions (CRs) with zero or one charged lepton, that are enriched
 156 in $Z \rightarrow \nu\nu$ and $W \rightarrow \ell\nu$ events, respectively. Additionally, CRs enriched in $t\bar{t}$ production
 157 events are also defined. The V + jets and $t\bar{t}$ production events in these CRs share many kine-
 158 matic properties of the processes in the SRs and are used to constrain the latter. The CR and SR
 159 definitions share as many of the selection criteria as possible, in order to ensure that minimal
 160 selection biases are introduced. Seven CRs are defined: six single-electron and single-muon
 161 CRs enriched in $W \rightarrow \ell\nu$ and $t\bar{t}$ production events, and a seventh CR enriched in $Z \rightarrow \nu\nu$
 162 production events.

163 The SR events are selected using a trigger with a p_T^{miss} requirement of at least 120 GeV. The
 164 trigger requirement for the SRs is based on an online calculation of p_T^{miss} based on all PF can-
 165 didates reconstructed at the HLT, except for muons. Events with high- p_T muons are there-
 166 fore also assigned large online p_T^{miss} , and the same trigger is used to collect data populating
 167 the single-muon and CRs. The control samples with electrons are selected based on two dif-
 168 ferent single-electron triggers requiring of $p_T > 27$ (35, 32) GeV for 2016 (2017, 2018) and
 169 $p_T > 105$ GeV (115) for 2016 (2017 and 2018), and on a single-photon trigger with a require-
 170 ment of $p_T > 200$ GeV (for 2017 and 2018 only). The single-electron triggers differ in their
 171 usage of isolation requirements: while the lower threshold trigger requires electrons to be well
 172 isolated, the higher-threshold trigger does not, which gives an improved efficiency at high p_T .
 173 Similarly, the single-photon trigger avoids the reliance on the online track reconstruction and
 174 increases the overall efficiency for electrons with $p_T > 200$ GeV. During the 2016 and 2017
 175 data taking, a gradual shift in the timing of the inputs of the ECAL L1 trigger in the region at
 176 $|\eta| > 2.0$ caused a specific trigger inefficiency. For events containing an electron or a photon (a
 177 jet) with $p_T \gtrsim 50$ (100) GeV in this region, the efficiency loss is up to $\approx 10\text{--}20\%$, depending on
 178 p_T , η , and time. This issue is known as the L1 pre-firing. Correction factors are computed from
 179 data and applied to the acceptance evaluated by simulation for the 2016 and 2017 samples.

180 At the analysis level, a requirement of $p_T^{\text{miss}} > 250$ GeV is applied to the SR events in order to
 181 ensure a p_T^{miss} trigger efficiency of at least 95%. The leading AK15 jet in p_T is required to have
 182 $p_T > 160$ GeV, $|\eta| < 2.4$, an SD-corrected mass (m_{SD}) of $40 < m_{\text{SD}} < 300$ GeV. In order to
 183 preferentially select events where the leading AK15 jet originates from a hadronic decay of a

184 dark Higgs boson, the jet is further required to be double-b tagged with the DEEPAK15 algo-
 185 rithm [37]. The DEEPAK15 algorithm employs a deep neural network to differentiate between
 186 jets from vector boson, top quark, and Higgs boson decays, as well as jets originating from
 187 QCD radiation. The inputs to the neural network are features of up to 100 jet constituent PF
 188 candidates of a given jet and features related to up to seven secondary vertices reconstructed in
 189 a given collision event. For each jet, the output of the neural network is one numerical score for
 190 each of the jet classes, representing the likelihood that the jet originates from that class. In this
 191 analysis, separation between dark Higgs bosons and QCD jets is sought, and a binary score is
 192 constructed by taking the ratio of the sum of the SM $Z \rightarrow bb$ and $H \rightarrow bb$ scores to the sum of
 193 the SM $Z \rightarrow bb$, $H \rightarrow bb$, and QCD scores.

194 Further requirements are imposed in order to suppress reducible background processes. Events
 195 are rejected if they contain a well-reconstructed and isolated electron (photon) with $p_T > 10$
 196 (15) GeV and $|\eta| < 2.5$ or a muon with $p_T > 10$ GeV and $|\eta| < 2.4$ [38, 39]. Hadronically de-
 197 caying τ leptons are identified using the DEEPTAU algorithm [40]. Events with a hadronically de-
 198 caying τ lepton candidate with $p_T > 20$ GeV and $|\eta| < 2.3$ are removed. These require-
 199 ments efficiently reject events with leptonic decays of the V bosons and top quarks, as well as
 200 backgrounds with photons. Contributions from top quark processes are further suppressed by
 201 rejecting events with AK4 jets that do not overlap with the leading AK15 jet, have $p_T > 20$ GeV
 202 and $|\eta| < 2.4$, and are identified to have originated from the hadronization of a bottom quark
 203 (“b-tagged jets”). The b-tagging of AK4 jets is performed using the DEEPJET algorithm [41]
 204 with a “loose” working point, corresponding to a probability of 10% of misidentifying a light-
 205 flavor quark or gluon jet. Finally, topological requirements are applied in order to reject con-
 206 tributions from QCD multijet events. These events do not have p_T^{miss} from genuine sources
 207 and require a p_T^{miss} mismeasurement in order to pass the SR selections, which can happen in
 208 two main ways. In the first case, the energy of a jet in the event could be misreconstructed
 209 either as a result of an interaction between the jet with poorly instrumented or inactive parts
 210 of the detector, or because of failures in the readout of otherwise functioning detector mod-
 211 ules. In these cases, artificial p_T^{miss} is generated with a characteristically small azimuthal angle
 212 difference between the misreconstructed jet \vec{p}_T and the \vec{p}_T^{miss} vectors. Such events are rejected
 213 by requiring the minimum azimuthal angle between the \vec{p}_T^{miss} direction and each AK4 jet in
 214 the event to be larger than 0.5 radians. With the same goal, the azimuthal angle between the
 215 \vec{p}_T^{miss} direction and each AK15 jet in the event must be larger than 1.5 radians. In the second
 216 case, large p_T^{miss} is generated due to failures of the PF reconstruction, which are suppressed by
 217 considering an alternative calculation of p_T^{miss} based on calorimeter energy clusters and muon
 218 candidates, rather than the full set of all PF candidates. While the calorimeter-based p_T^{miss}
 219 has significantly worse resolution than PF p_T^{miss} , it is much simpler and more robust. To re-
 220 duce the multijet background caused by PF reconstruction failures, events are required to have
 221 $\Delta p_T^{\text{miss}}(\text{PF-calorimeter}) = |p_T^{\text{miss}}(\text{PF})/p_T^{\text{miss}}(\text{calorimeter}) - 1| < 0.5$. Finally, a section of the
 222 HCAL was not functioning during a part of the 2018 data taking period corresponding to 65%
 223 of the total integrated luminosity recorded in that year, leading to irrecoverable mismeasure-
 224 ment in a localized region of the detector ($-1.57 < \phi < -0.87$, $-3.0 < \eta < -1.3$). To avoid
 225 contamination from such mismeasurement, events where any jet with $p_T > 30$ GeV is found in
 226 the corresponding η - ϕ region are rejected in the analysis of the 2018 data set. Events where the
 227 mismeasurement is so severe that a jet is fully lost in this region are found to contribute at low
 228 values of $p_T^{\text{miss}} < 470$ GeV and to have a characteristic signature in $\phi(\vec{p}_T^{\text{miss}})$. Such events are
 229 rejected by requiring that $\phi(\vec{p}_T^{\text{miss}}) \notin [-1.62, -0.62]$ if $p_T^{\text{miss}} < 470$ GeV. Expected yields from
 230 different processes in SR are reported in Table 1.

231 A control region (labelled as “ZCR”) composed of those events that satisfy all the SR require-

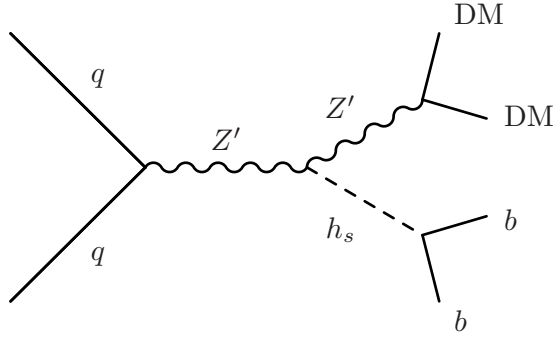


Figure 1: Feynman diagram for the production of a dark Higgs boson in association with DM particles.

Table 1: Expected yields from background processes in the signal region. Values are pre-fit and uncertainties are statistical-only.

	2016	2017	2018
$H \rightarrow b\bar{b}$	57.6 ± 0.3	72.0 ± 0.3	83.8 ± 0.3
$Z(\rightarrow \ell\ell) + \text{jets}$	56.8 ± 2.2	43.3 ± 2.0	37.1 ± 3.0
QCD multijet	93.3 ± 25.8	154.9 ± 41.7	163.2 ± 64.6
Diboson	718.0 ± 17.5	623.4 ± 17.8	606.4 ± 20.8
Single t	646.0 ± 10.9	567.4 ± 12.5	614.6 ± 12.8
$t\bar{t}$	5486.5 ± 199.7	5810.7 ± 60.0	6784.2 ± 133.7
$W(\rightarrow \ell\nu) + \text{jets}$	3997.8 ± 38.5	2991.0 ± 40.2	2826.6 ± 50.5
$Z(\rightarrow \nu\nu) + \text{jets}$	7514.8 ± 29.2	7035.2 ± 33.3	6978.5 ± 38.8
Total expected	18570.7 ± 208.1	17297.9 ± 92.4	18094.2 ± 163.4
$m_{Z'} = 1000 \text{ GeV}, m_{h_s} = 130 \text{ GeV}, m_{DM} = 150 \text{ GeV}$	684.8 ± 4.1	626.7 ± 3.9	687.2 ± 4.6
$m_{Z'} = 1000 \text{ GeV}, m_{h_s} = 130 \text{ GeV}, m_{DM} = 500 \text{ GeV}$	$(381.6 \pm 2.1) \times 10^{-4}$	$(357.6 \pm 2.0) \times 10^{-4}$	$(399.6 \pm 2.4) \times 10^{-4}$
$m_{Z'} = 1000 \text{ GeV}, m_{h_s} = 130 \text{ GeV}, m_{DM} = 1000 \text{ GeV}$	$(1341.2 \pm 6.7) \times 10^{-8}$	$(1005.9 \pm 6.7) \times 10^{-8}$	$(1341.2 \pm 10.1) \times 10^{-8}$

232 ments, but have the leading AK15 jet failing the DEEPAK15 selection, is used to constrain
 233 $Z(\nu\nu) + \text{jets}$ production in SR. Single-lepton CRs (labelled as “WEPCR” and “WMPCR”) are
 234 used to constrain $W(\ell\nu) + \text{jets}$ events in SR. The same selection criteria are applied to these
 235 CRs as for the SR, with the exception of the charged-lepton rejection criteria being inverted to
 236 allow for exactly one muon or one electron. The \vec{p}_T^{miss} vector used in the SR definition is re-
 237 placed by the hadronic recoil vector \vec{U} . The hadronic recoil is defined as the vectorial sum of
 238 the \vec{p}_T^{miss} vector and the transverse momentum vectors of the selected charged lepton in each
 239 event. The hadronic recoil therefore acts as a proxy of the momentum of the W boson in each
 240 CR, convolved with the p_T^{miss} resolution, which is equivalent to the role of p_T^{miss} in the SR. In
 241 order to enhance the purity of the CRs, specific additional selection criteria are applied. For
 242 the charged-lepton CRs, at least one of the leptons is required to pass a more strict set of qual-
 243 ity criteria and have $p_T > 40$ (20) GeV electrons (muons). Additionally, in the single-electron
 244 CR are required to have $p_T^{\text{miss}} > 100$ GeV in order to reject contributions from QCD multi-
 245 jet events. Additional single-lepton CRs (labelled as “WEFCR” and “WMFCR”) composed of
 246 those single-lepton events with the leading AK15 jet failing the DEEPAK15 selection are also
 247 used to constrain $W(\ell\nu) + \text{jets}$ events in SR. Finally, in order to select single-lepton events en-
 248 riched in $t\bar{t}$ production, additional CRs (labelled as “TECR” and “TMCR”) are identified by
 249 inverting the veto on b-tagged AK4 jets outside the leading AK15 jet cone.

250 The selection criteria that define the different SR and CRs are summarized in Table 2.

251 **4 Background estimation**

252 Background estimation and signal extraction are performed simultaneously, using a joint max-
 253 imum likelihood (ML) fit across all SR and CRs. A likelihood function is constructed to model
 254 the expected background contributions in each bin of the two-dimensional recoil-vs- m_{SD} vari-
 255 able of the SR and CRs, as well as the expected signal yield in each bin of the SR. The best fit
 256 background model, as well as the best fit signal strength, are obtained by maximizing the joint
 257 likelihood function of all categories.

258 **4.1 Likelihood function**

259 The likelihood function maximized by the fit is:

$$\begin{aligned}
\mathcal{L}_c(\mu_{ZCR}^Z, \mu_{SR}^{t\bar{t}}, \mu, \theta) = & \prod_{i,j} \text{Poisson} \left(d_{i,j}^{ZCR} | B_{i,j}^{ZCR}(\theta) + (1 + R^{W-Z})_{i,j}(\theta) \mu_{ZCR,i,j}^Z \right) \\
& \times \prod_{i,j} \text{Poisson} \left(d_{i,j}^{TTECR} | B_{i,j}^{TTECR}(\theta) + \frac{\mu_{SR,i,j}^{t\bar{t}}}{R_{TTECR,i,j}^{t\bar{t}}(\theta)} \right) \\
& \times \prod_{i,j} \text{Poisson} \left(d_{i,j}^{TTMCR} | B_{i,j}^{TTMCR}(\theta) + \frac{\mu_{SR,i,j}^{t\bar{t}}}{R_{TTMCR,i,j}^{t\bar{t}}(\theta)} \right) \\
& \times \prod_{i,j} \text{Poisson} \left(d_{i,j}^{WEFCR} | B_{i,j}^{WEFCR}(\theta) + \frac{R^{W-Z}_{i,j}(\theta) \mu_{ZCR,i,j}^Z}{R_{WEFCR,i,j}^W(\theta)} \right) \\
& \times \prod_{i,j} \text{Poisson} \left(d_{i,j}^{WMFCR} | B_{i,j}^{WMFCR}(\theta) + \frac{R^{W-Z}_{i,j}(\theta) \mu_{ZCR,i,j}^Z}{R_{WMFCR,i,j}^W(\theta)} \right) \\
& \times \prod_{i,j} \text{Poisson} \left(d_{i,j}^{WEPCR} | B_{i,j}^{WEPCR}(\theta) + \frac{R_{p/f,i,j}^W(\theta) R^{W-Z}_{i,j}(\theta) \mu_{ZCR,i,j}^Z}{R_{WEPCR,i,j}^W(\theta)} + \frac{\mu_{SR,i,j}^{t\bar{t}}}{R_{WEPCR,i,j}^{t\bar{t}}(\theta)} \right) \\
& \times \prod_{i,j} \text{Poisson} \left(d_{i,j}^{WMPCR} | B_{i,j}^{WMPCR}(\theta) + \frac{R_{p/f,i,j}^W(\theta) R^{W-Z}_{i,j}(\theta) \mu_{ZCR,i,j}^Z}{R_{WMPCR,i,j}^W(\theta)} + \frac{\mu_{SR,i,j}^{t\bar{t}}}{R_{WMPCR,i,j}^{t\bar{t}}(\theta)} \right) \\
& \times \prod_i \text{Poisson} \left(d_{i,j}^{SR} | B_{i,j}^{SR}(\theta) + (R_{p/f,i,j}^Z(\theta) + R_{p/f,i,j}^W(\theta) R^{W-Z}_{i,j}(\theta)) \mu_{ZCR,i,j}^Z + \mu_{SR,i,j}^{t\bar{t}} + \mu S_{i,j}(\theta) \right)
\end{aligned} \tag{1}$$

260 In the above likelihood, $d_{i,j}^{*R}$ are the observed number of events in each (i,j) bin of the two-
261 dimensional recoil-vs- m_{SD} distribution in the SR and CRs, while $B_{i,j}^{*R}$ is the number of back-
262 ground events. The parameter μ_{ZCR}^Z represents the yield of the $Z \rightarrow \nu\nu + \text{jets}$ background in
263 the ZCR, and is left freely floating in the fit. The parameter $\mu_{SR}^{t\bar{t}}$ represents the yield of the $t\bar{t}$
264 background in the SR, that is left freely floating in the fit as well. The likelihood also includes
265 the SR with μ being the signal strength parameter also left floating in the fit. The systematic
266 uncertainties (θ) enter the likelihood as additive perturbations to the transfer factors R used in
267 the modeling of the main backgrounds, as well as to the minor background and signal expec-
268 tations, and are modeled as Gaussians.

269 Separate approaches are adopted to estimate the dominant ($Z + \text{jets}$, $W + \text{jets}$, $t\bar{t}$) and subdom-
270 inant (single top, diboson, Higgs, and QCD multijet) backgrounds.

271 The predictions for the dominant $Z + \text{jets}$ and $W + \text{jets}$ backgrounds are based on the yield of
272 $Z \rightarrow \nu\nu$ events in each bin of the ZCR. The per-bin yields for this process are defined as free
273 parameters of the likelihood function. The yields for the $Z + \text{jets}$ and $W + \text{jets}$ contribution
274 to the SR, as well as the yields of the $W + \text{jets}$ process in the CRs are defined relative to the
275 $Z \rightarrow \nu\nu$ yields by introducing a set of per-bin transfer factors. The yields of $t\bar{t}$ events in the
276 single-lepton CRs are similarly related via transfer factors to the $t\bar{t}$ event yields in the SRs. This
277 choice of transfer factors takes into account the correlations between the $V + \text{jets}$ background
278 contributions in all regions. In all cases, the central values of the transfer factors are obtained
279 from the ratios of the simulated recoil-vs- m_{SD} spectra of the respective processes in the SRs to

280 those in CRs. For the minor backgrounds the nominal expected yield per region is obtained
281 directly from simulation.

282 Systematic uncertainties are incorporated in the likelihood function as nuisance parameters,
283 as described in more detail below. In the case of the $V + \text{jets}$ and $t\bar{t}$ processes, the nuisance
284 parameters affect the values of the transfer factors in each recoil-vs- m_{SD} variable bin and thus
285 control the ratios of the contributions from different processes, as well as the ratios of the yields
286 in the SRs to those in various CRs. For the subdominant background processes, the yields in
287 each bin are directly parameterized in terms of the nuisance parameters. The final free pa-
288 rameter of the likelihood function is the signal strength modifier μ , which—for a given signal
289 hypothesis—controls the signal normalization relative to the theoretical cross section.

290 The likelihood method relies on the accurate predictions of the ratios between the dominant
291 backgrounds in the SRs and CRs, as well as on the absolute normalization and shape of the
292 recoil-vs- m_{SD} distributions for the subdominant backgrounds. To achieve the most accurate
293 possible predictions for these quantities, weights are applied to each simulated event to take
294 into account both experimental and theoretical effects not present in the MC simulated sam-
295 ples. The experimental corrections are related to the trigger efficiencies, identification and
296 reconstruction efficiencies of charged leptons and of b-tagged and doubleb-tagged jets, and
297 the pileup distribution in simulation. Theoretical corrections are applied to the $V + \text{jets}$ pro-
298 cesses in order to model the effects of NLO terms in the perturbative EW corrections [42]. The
299 corrections are parameterized as functions of the generator-level boson p_{T} and are evaluated
300 separately for the $W(\ell\nu) + \text{jets}$ and $Z(\ell\ell) + \text{jets}$ processes.

301 **4.2 Systematic uncertainties**

302 The inputs to the ML fit are subject to various experimental and theoretical uncertainties. Un-
303 certainties in the measurement of the integrated luminosity in each year of data taking are
304 0.6–2%. The uncertainties in the corrections for the L1 pre-firing effect in 2016 and 2017, as
305 well as the uncertainties in the pile up correction are of the order of 1%. The uncertainties in
306 the efficiencies of reconstructing and identifying electron candidates are 1% and 2–3%, respec-
307 tively. For muons, the uncertainties in the identification efficiency are 1%, with an additional
308 1% uncertainty in the efficiency of the isolation criteria. A systematic uncertainty for each lep-
309 ton/photon veto selection has been obtained by propagating the overall uncertainties in the
310 identification of muons, electrons, photons, and taus, into the vetoed regions. While the un-
311 certainties are found to be negligible for photon, muon, and electron vetoes, a 3% uncertainty
312 in the tau veto is included. The uncertainties in the trigger efficiency are 1% for the single
313 electron trigger and 1–2% for the $p_{\text{T}}^{\text{miss}}$ trigger. The uncertainty in the modeling of $p_{\text{T}}^{\text{miss}}$ in sim-
314 ulation [43] is dominated by the uncertainty in the jet energy corrections. The resulting bin
315 migration affects the acceptance of the minimum requirement in $p_{\text{T}}^{\text{miss}}$. The change in rate is
316 estimated to be 5% and it is included as a systematic uncertainty. An additional systematic un-
317 certainty is included to cover the effect of the uncertainties in the AK15 jet energy corrections
318 on the AK15 jet p_{T} . Also in this case, the resulting bin migration affects the acceptance of the
319 minimum requirements in AK15 jet p_{T} . This introduces an effect on the rate of the order of 4%.
320 The uncertainty in the b-tagging efficiency leads to a shape uncertainty applied to all processes
321 in all regions. The uncertainty in the doubleb-tagging efficiency results in a shape uncertainty
322 applied to the signal processes in SR. Uncertainties of 100% are assigned to the normalization
323 of the QCD multijet background contributions in the all regions. These uncertainties are corre-
324 lated between regions with the same source of fake: one uncertainty is applied to QCD multijet
325 events in the SR and in the ZCR, a separate uncertainty is applied to QCD multijet events in the
326 single-muon CRs, and similarly for the single-electron CRs. Additionally, uncertainties of 20%

327 are assigned to the cross section of diboson, SM Higgs boson, and $Z(\rightarrow \ell\ell)$ +jets productions.
 328 Similarly, 10% uncertainties in the single top quark and $t\bar{t}$ production cross sections are also
 329 assigned. The theoretical uncertainties in the transfer factors related to higher-order effects in
 330 the QCD and EW perturbative expansions are calculated according to the prescription given
 331 in Ref. [42] and implemented, as described in Ref. [44]. Bin-by-bin statistical uncertainties are
 332 incorporated following the Barlow-Beeston-lite approach [45].

333 The likelihood functions obtained for the three data taking years are combined in order to max-
 334 imize the statistical power of the analysis. The combination is performed by defining a com-
 335 bined likelihood describing all the analysis regions in all data sets. For this purpose, the effects
 336 of all theoretical uncertainties are assumed to be correlated. Most experimental uncertainties
 337 are dominated by the inherent precision of auxiliary measurements specific to each data set
 338 and are thus assumed to be uncorrelated between different data taking years. The experimen-
 339 tal uncertainties related to the determination of the integrated luminosity and to the b-tagging
 340 efficiency are partially correlated between the data taking years, which is taken into account by
 341 splitting the total uncertainty into its correlated and uncorrelated components.

342 5 Results and interpretation

343 The ML fit is performed by combining the analysis categories as well as the data sets corre-
 344 sponding to the different years of data taking. The recoil-vs- m_{SD} distributions in SR and CRs
 345 before (“pre-fit”) and after (“post-fit”) the fit are shown in Figs. 2-16. In all cases, good agree-
 346 ment is observed between the background-only post-fit result and the data.

347 Signal strength exclusion limits are presented for different signal hypotheses. All data sets and
 348 categories are included. The exclusion limits are calculated using the asymptotic approxima-
 349 tion of the CL_s method [46–48]. In this method, a signal-plus-background fit is performed for
 350 each signal hypothesis in addition to the background-only fit. In the signal fits, the nuisance
 351 parameters are profiled, and the resulting best fit nuisance parameters vary for the different
 352 signal hypotheses. Consequently, different nonzero best fit values for the signal strength can
 353 be obtained for different signals even if the background-only fit succeeds in modeling the data.
 354 In the exclusion limits, this feature is represented by differences between the observed and
 355 expected limits.

356 Exclusion limits are calculated in the two-dimensional parameter space of the DM and medi-
 357 ator masses, m_{DM} and m_{med} . The coupling between the mediator and SM quarks is set to a
 358 constant value of $g_q = 0.25$, and the mediator-DM coupling is set to $g_\chi = 1.0$. The resulting
 359 exclusion limits at 95% confidence level (CL) on the signal strength μ are shown in Figs. 17-18
 360 for different hypotheses of the dark Higgs boson mass. For small values of $m_{DM} \approx 1$ GeV dif-
 361 ferent values of the mediator mass m_{med} are expected to be excluded as a function of the dark
 362 Higgs boson mass. The excluded value of m_{med} reduces with increasing values of m_{DM} , as the
 363 branching fraction for decays of the mediator into dark matter candidates is reduced.

364 The constraints placed on the dark Higgs boson production model imply bounds on the inter-
 365 action cross section between DM candidates and nuclei. The fixed-coupling exclusion curves
 366 at 90% CL in the m_{med} - m_{DM} plane are translated point-by-point using the formulae described
 367 in Ref. [49], which depend on the coupling choices $g_q = 0.25$ and $g_\chi = 1.0$ and on the specific
 368 signal model. The resulting curves in the m_{DM} - $\sigma_{DM\text{-nucleon}}$ plane are compared to the results
 369 from DD experiments in Figs. ??-?. Qualitatively, although model dependent, the results from
 370 this search depend on m_{DM} only weakly (as long as $m_{DM} < m_{med}/2$), leading to stringent con-
 371 straints also at low values of m_{DM} . The sensitivity of most DD experiments is limited in this

Table 2: Summary of cuts that define the different analysis regions.

Selection	SR	ZCR	WMPCR	WEPCR	WMFCR	WEFCR	TTMCR	TTECR
$U > 250 \text{ GeV}$	✓	✓	✓	✓	✓	✓	✓	✓
$\Delta p_T^{\text{miss}}(\text{PF-calorimeter}) > 0.5$	✓	✓	✓	✓	✓	✓	✓	✓
Leading AK15 $p_T > 160 \text{ GeV}$	✓	✓	✓	✓	✓	✓	✓	✓
Leading AK15 $m_{SD} \in [40, 300] \text{ GeV}$	✓	✓	✓	✓	✓	✓	✓	✓
$\min \Delta\phi(\vec{U}, \vec{AK4s}) > 0.5$	✓	✓	✓	✓	✓	✓	✓	✓
$\min \Delta\phi(\vec{U}, \vec{AK15s}) > 1.5$	✓	✓	✓	✓	✓	✓	✓	✓
$p_T^{\text{miss}} > 100 \text{ GeV}$	✗	✗	✗	✓	✗	✓	✗	✓
# of muons	0	0	1	0	1	0	1	0
# of electrons	0	0	0	1	0	1	0	1
# of photons	0	0	0	0	0	0	0	0
# of taus	0	0	0	0	0	0	0	0
# of extra b-tagged AK4s	0	0	0	0	0	0	≥ 1	≥ 1
DeepAK15 > wp(90% signal eff.)	pass	fail	pass	pass	fail	fail	pass	pass

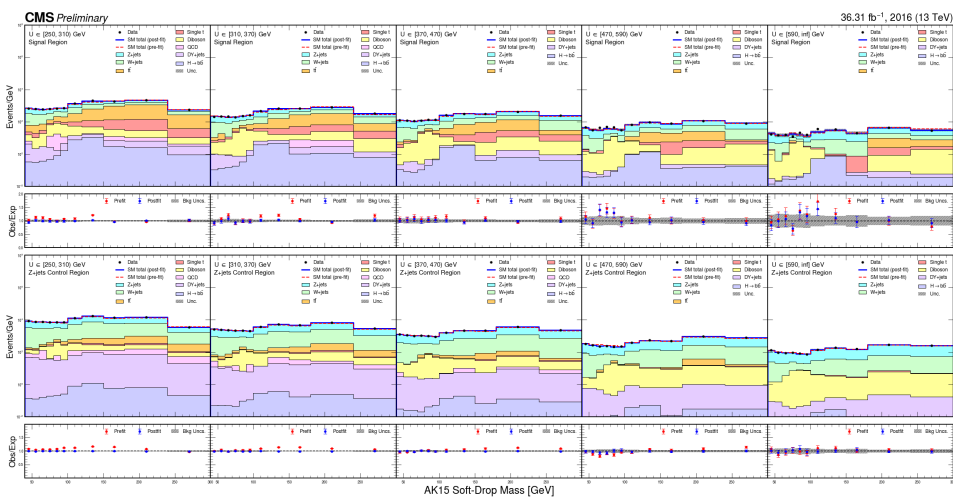


Figure 2: Post-fit m_{SD} distributions in bins of U . Top, distributions in signal region; bottom, distributions in Z+jets control region.

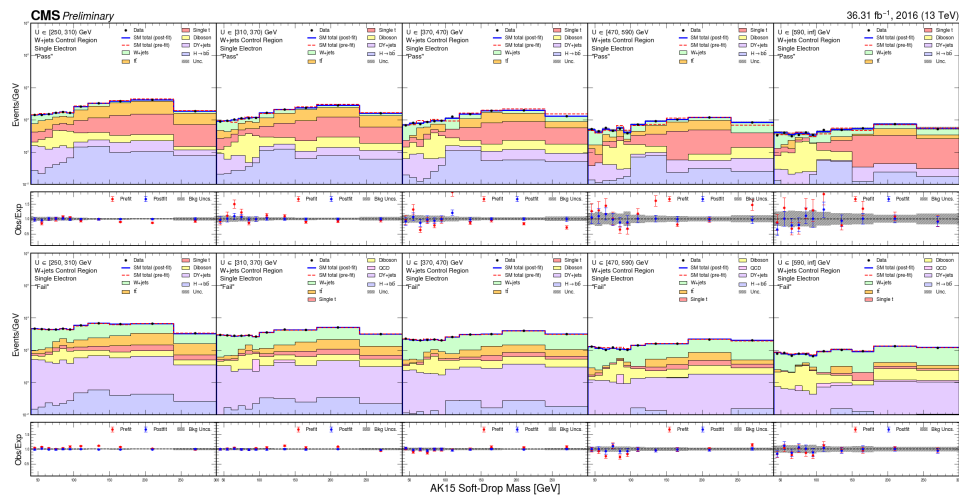


Figure 3: Post-fit m_{SD} distributions in bins of U . Top, distributions in W+jets single electron “pass” control region; bottom, distributions in W+jets single electron “fail” control region.

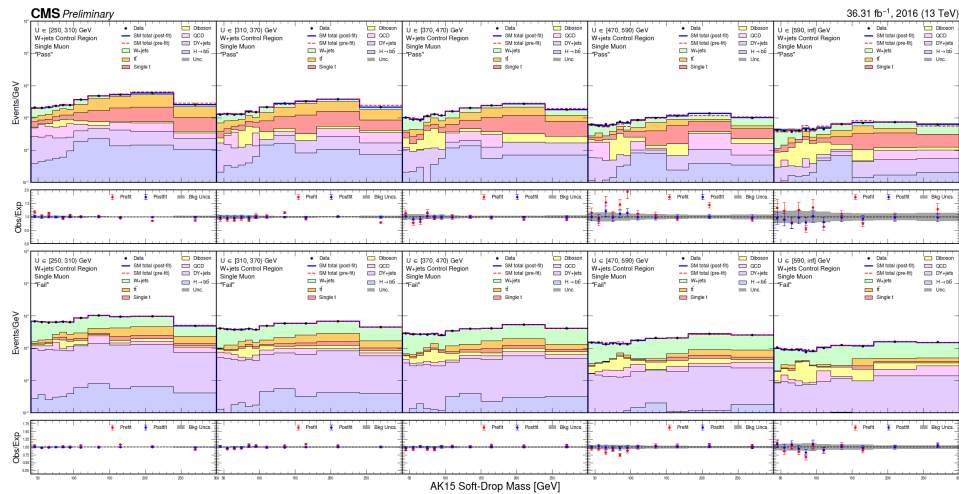


Figure 4: Post-fit m_{SD} distributions in bins of U . Top, distributions in W+jets single muon “pass” control region; bottom, distributions in W+jets single muon “fail” control region.

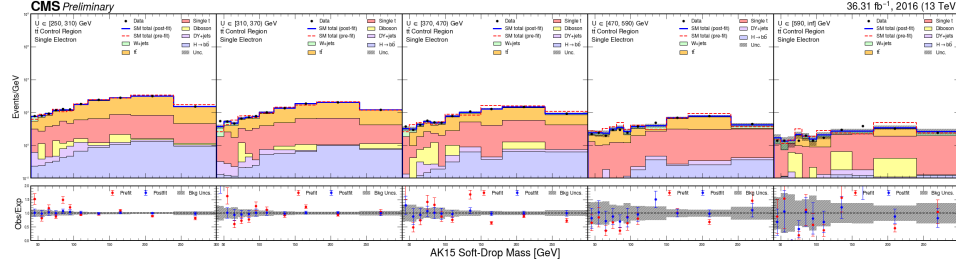


Figure 5: Post-fit m_{SD} distributions in bins of U in $t\bar{t}$ single electron control region.

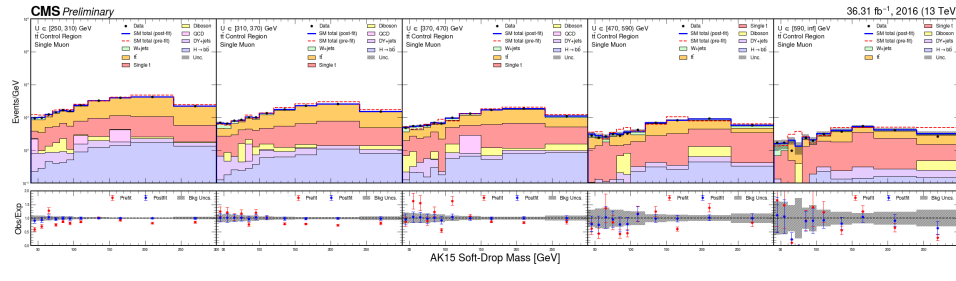


Figure 6: Post-fit m_{SD} distributions in bins of U in $t\bar{t}$ single muon control region.

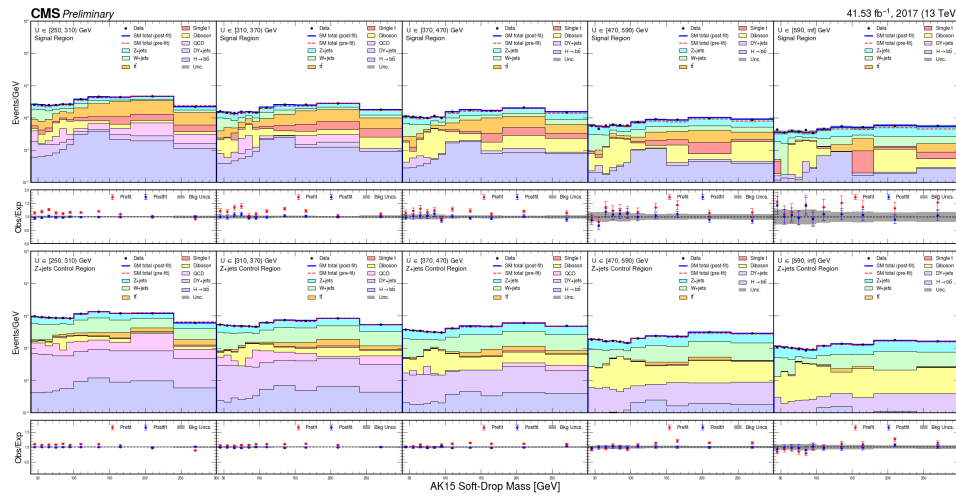


Figure 7: Post-fit m_{SD} distributions in bins of U . Top, distributions in signal region; bottom, distributions in Z+jets control region.

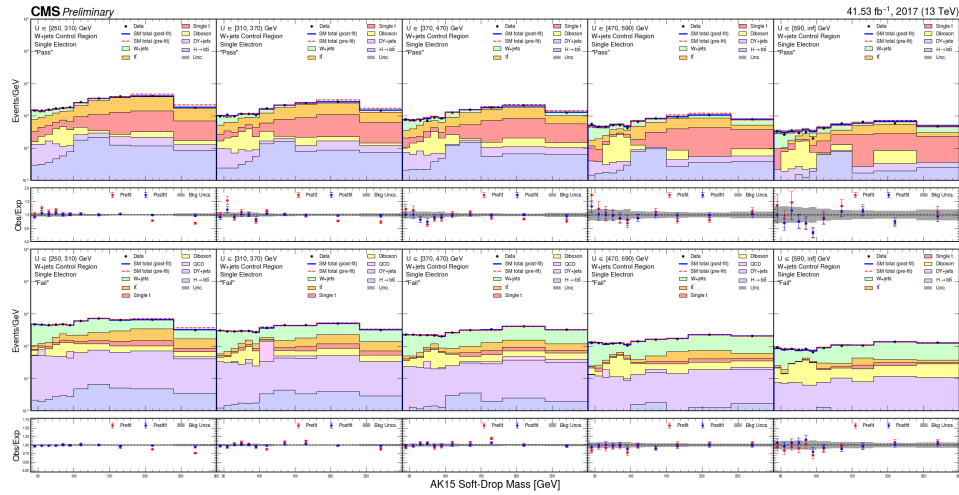


Figure 8: Post-fit m_{SD} distributions in bins of U . Top, distributions in W+jets single electron “pass” control region; bottom, distributions in W+jets single electron “fail” control region.

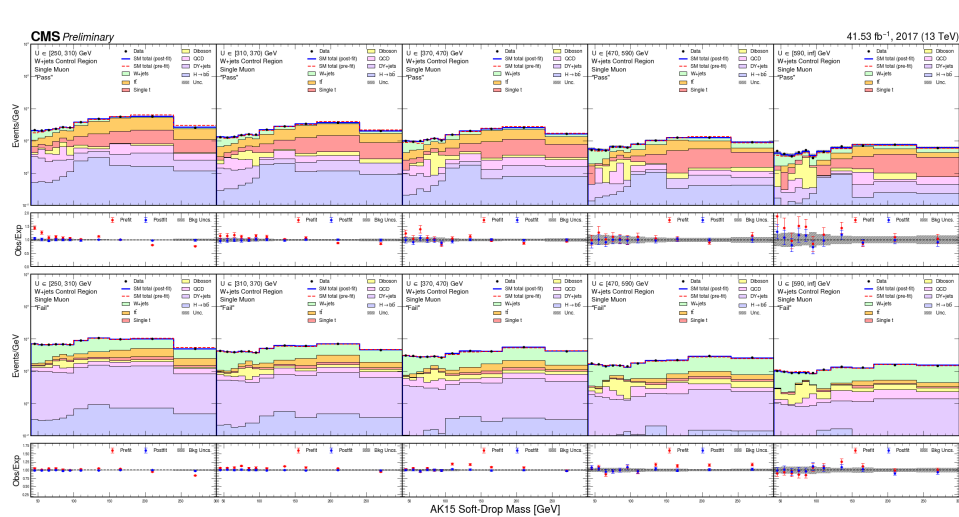


Figure 9: Post-fit m_{SD} distributions in bins of U . Top, distributions in W+jets single muon “pass” control region; bottom, distributions in W+jets single muon “fail” control region.

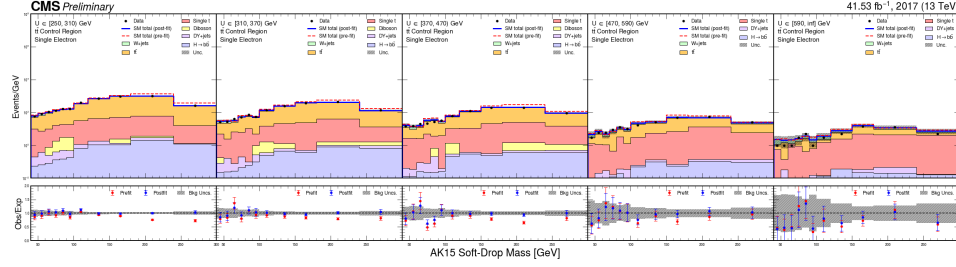


Figure 10: Post-fit m_{SD} distributions in bins of U in $t\bar{t}$ single electron control region.

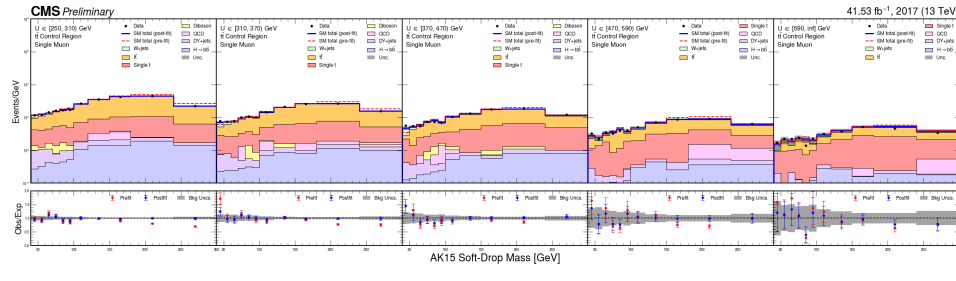


Figure 11: Post-fit m_{SD} distributions in bins of U in $t\bar{t}$ single muon control region.

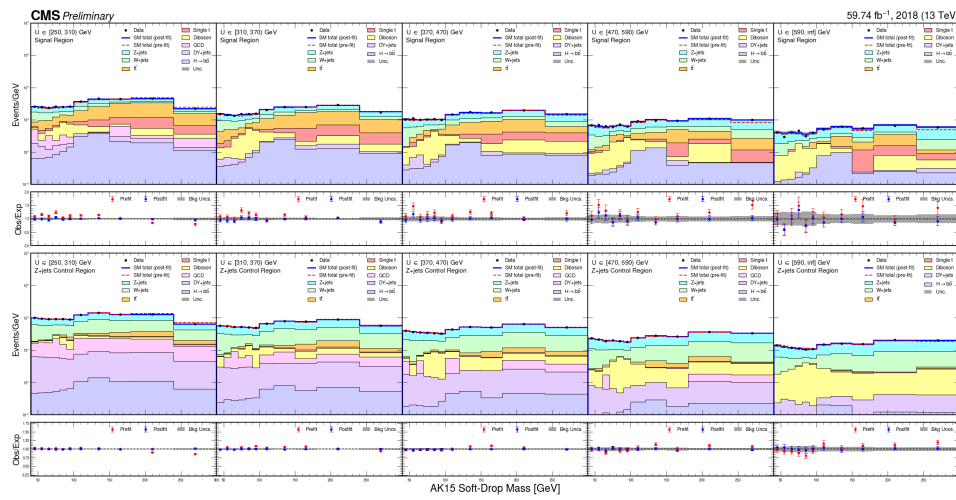


Figure 12: Post-fit m_{SD} distributions in bins of U . Top, distributions in signal region; bottom, distributions in Z+jets control region.

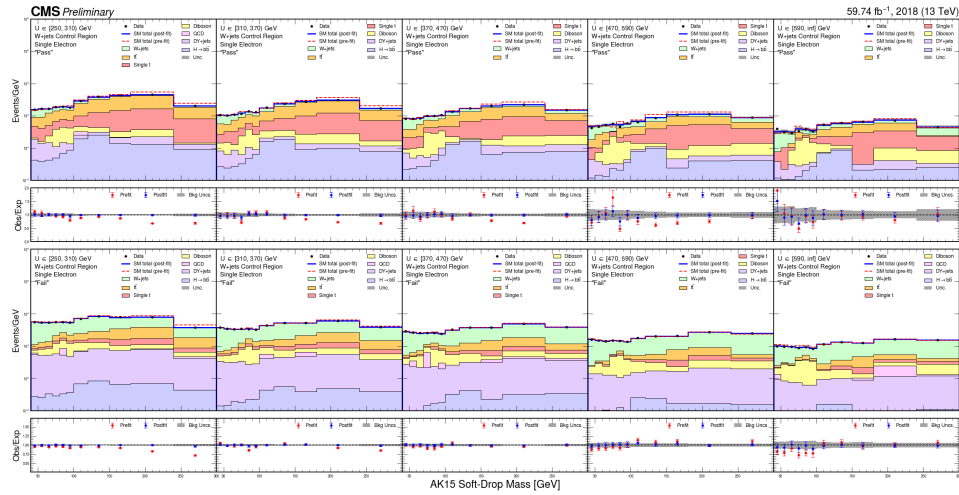


Figure 13: Post-fit m_{SD} distributions in bins of U . Top, distributions in W+jets single electron “pass” control region; bottom, distributions in W+jets single electron “fail” control region.

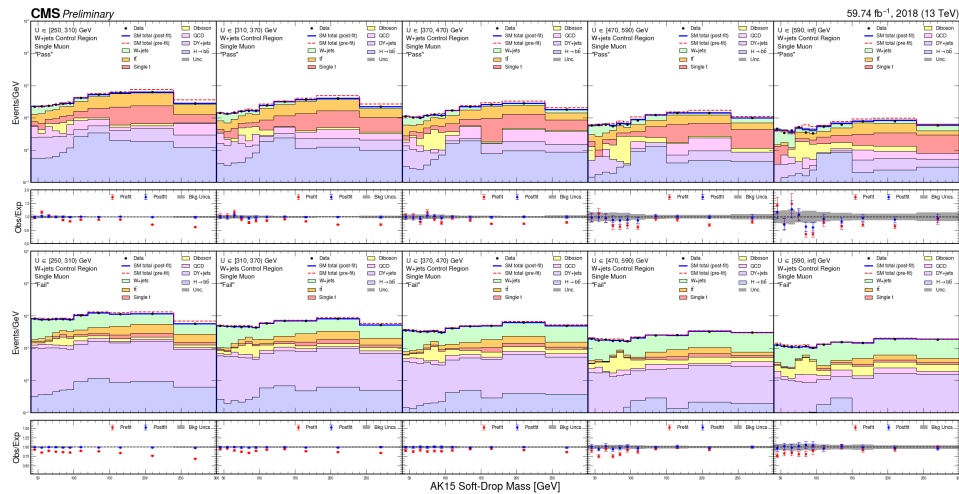


Figure 14: Post-fit m_{SD} distributions in bins of U . Top, distributions in W+jets single muon “pass” control region; bottom, distributions in W+jets single muon “fail” control region.

regime as the small value of m_{DM} translates into a reduced signal-to-noise ratio relative to the case of more massive DM. Depending on the mediator type, the resulting couplings between DM particles and nuclei are either spin dependent (axial-vector) or independent (vector). In the spin-dependent case, the sensitivity of DD experiments is limited relative to collider searches as the DM-nucleus scattering is no longer coherent.

6 Summary

A search for physics beyond the standard model in events with a large-cone energetic jet consistent with the hadronization of a resonant b-quark pair and large missing transverse momentum has been presented. A data set of proton-proton collisions at a center-of-mass energy of 13 TeV, corresponding to an integrated luminosity of 137.2 fb^{-1} is analyzed. A joint maximum likelihood fit over a combination of signal and control regions is used to constrain standard model (SM) background processes and to extract a possible signal. The result is interpreted in terms of exclusion limits at 95% confidence level on the parameters of a model of production of a dark Higgs boson in association with dark matter particles. Values of the mediator mass of up to 2.5–4.5 TeV are excluded, depending on the mass of the dark Higgs boson and assuming the couplings of $g_q = 0.25$ between the mediator and quarks, and $g_\chi = 1.0$ between the mediator and the DM particles.

Acknowledgments

References

- [1] G. Bertone, D. Hooper, and J. Silk, “Particle dark matter: evidence, candidates and constraints”, *Phys. Rept.* **405** (2005) 279, doi:10.1016/j.physrep.2004.08.031, arXiv:hep-ph/0404175.
- [2] D. Abercrombie et al., “Dark matter benchmark models for early LHC Run-2 searches: report of the ATLAS/CMS dark matter forum”, 2015. arXiv:1507.00966.
- [3] CMS Collaboration, “Search for new particles in events with energetic jets and large missing transverse momentum in proton-proton collisions at $\sqrt{s} = 13 \text{ TeV}$ ”, *JHEP* **11** (2021) 153, doi:10.1007/JHEP11(2021)153, arXiv:2107.13021.
- [4] ATLAS Collaboration, “Search for new phenomena in events with an energetic jet and missing transverse momentum in pp collisions at $\sqrt{s} = 13 \text{ TeV}$ with the ATLAS detector”, *Phys. Rev. D* **103** (2021), no. 11, 112006, doi:10.1103/PhysRevD.103.112006, arXiv:2102.10874.
- [5] M. Duerr et al., “Hunting the dark higgs”, *Journal of High Energy Physics* **2017** (2017), no. 4, 143, doi:10.1007/JHEP04(2017)143.
- [6] ATLAS Collaboration, “Search for dark matter produced in association with a dark Higgs boson decaying into W^+W^- in the one-lepton final state at $\sqrt{s}=13 \text{ TeV}$ using 139 fb^{-1} of pp collisions recorded with the ATLAS detector”, *JHEP* **07** (2023) 116, doi:10.1007/JHEP07(2023)116, arXiv:2211.07175.
- [7] CMS Collaboration, “Search for dark matter particles in W^+W^- events with transverse momentum imbalance in proton-proton collisions at $\sqrt{s} = 13 \text{ TeV}$ ”, arXiv:2310.12229.

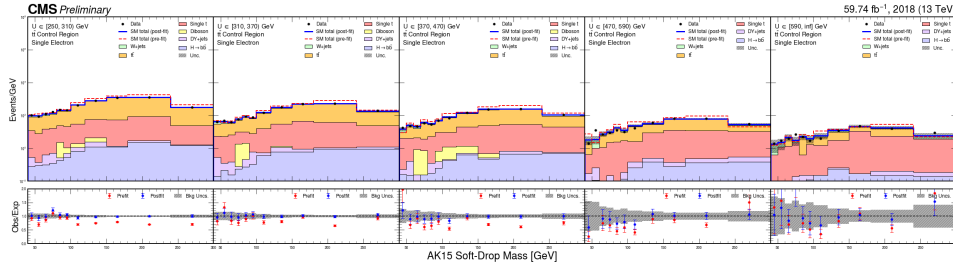


Figure 15: Post-fit m_{SD} distributions in bins of U in $t\bar{t}$ single electron control region.

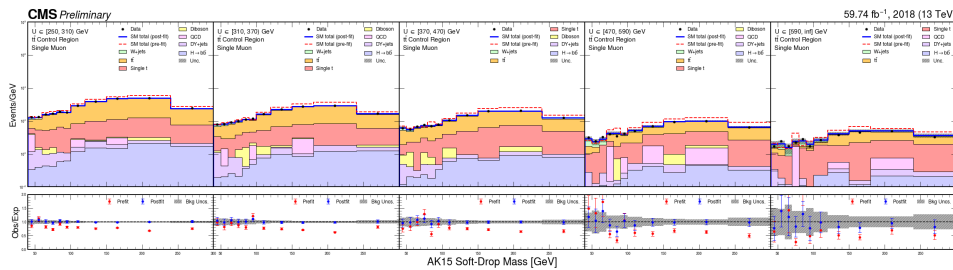


Figure 16: Post-fit m_{SD} distributions in bins of U in $t\bar{t}$ single muon control region.

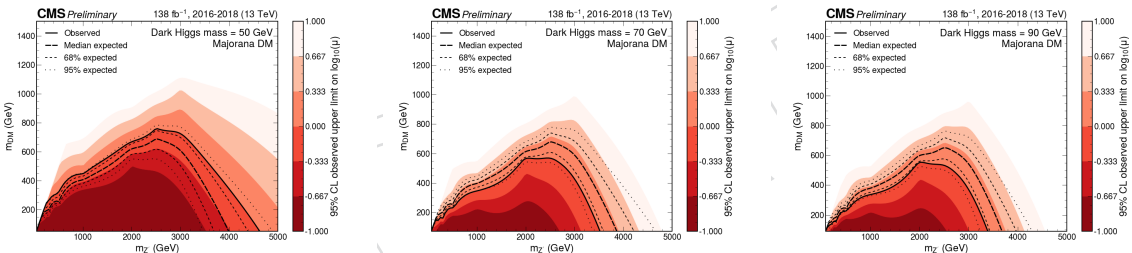


Figure 17: Expected and observed exclusion limits at 95% CL on the signal strength $\mu = \sigma/\sigma_{\text{theo}}$ as a function of m_{med} for a dark Higgs boson mass of 50 GeV (left), 70 GeV (middle), and 90 GeV (right). The black solid line indicates the exclusion boundary $\mu = 1$. Parameter combinations with larger values of μ are excluded.

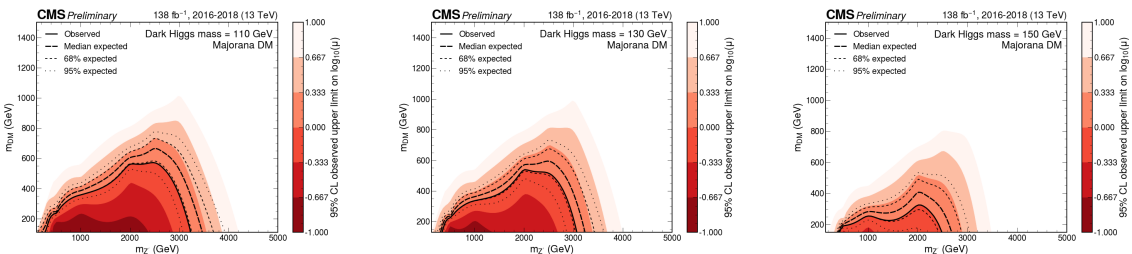


Figure 18: Expected and observed exclusion limits at 95% CL on the signal strength $\mu = \sigma/\sigma_{\text{theo}}$ as a function of m_{med} for a dark Higgs boson mass of 110 GeV (left), 130 GeV (middle), and 150 GeV (right). The black solid line indicates the exclusion boundary $\mu = 1$. Parameter combinations with larger values of μ are excluded.

- [8] CMS Collaboration, “Performance of the CMS Level-1 trigger in proton-proton collisions at $\sqrt{s} = 13$ TeV”, *JINST* **15** (2020) P10017, doi:10.1088/1748-0221/15/10/P10017, arXiv:2006.10165.
- [9] CMS Collaboration, “The CMS trigger system”, *JINST* **12** (2017) P01020, doi:10.1088/1748-0221/12/01/P01020, arXiv:1609.02366.
- [10] CMS Collaboration, “The CMS experiment at the CERN LHC”, *JINST* **3** (2008) S08004, doi:10.1088/1748-0221/3/08/S08004.
- [11] M. Cacciari, G. P. Salam, and G. Soyez, “The anti- k_t jet clustering algorithm”, *JHEP* **04** (2008) 063, doi:10.1088/1126-6708/2008/04/063, arXiv:0802.1189.
- [12] M. Cacciari, G. P. Salam, and G. Soyez, “FastJet user manual”, *Eur. Phys. J. C* **72** (2012) 1896, doi:10.1140/epjc/s10052-012-1896-2, arXiv:1111.6097.
- [13] CMS Collaboration, “Particle-flow reconstruction and global event description with the CMS detector”, *JINST* **12** (2017) P10003, doi:10.1088/1748-0221/12/10/P10003, arXiv:1706.04965.
- [14] CMS Collaboration, “Performance of missing transverse momentum reconstruction in proton-proton collisions at $\sqrt{s} = 13$ TeV using the CMS detector”, *JINST* **14** (2019) P07004, doi:10.1088/1748-0221/14/07/P07004, arXiv:1903.06078.
- [15] CMS Collaboration, “Jet energy scale and resolution in the CMS experiment in pp collisions at 8 TeV”, *JINST* **12** (2017) P02014, doi:10.1088/1748-0221/12/02/P02014, arXiv:1607.03663.
- [16] CMS Collaboration, “Jet algorithms performance in 13 TeV data”, CMS Physics Analysis Summary CMS-PAS-JME-16-003, 2017.
- [17] D. Bertolini, P. Harris, M. Low, and N. Tran, “Pileup per particle identification”, *JHEP* **10** (2014) 059, doi:10.1007/JHEP10(2014)059, arXiv:1407.6013.
- [18] M. Dasgupta, A. Fregoso, S. Marzani, and G. P. Salam, “Towards an understanding of jet substructure”, *JHEP* **09** (2013) 029, doi:10.1007/JHEP09(2013)029, arXiv:1307.0007.
- [19] J. M. Butterworth, A. R. Davison, M. Rubin, and G. P. Salam, “Jet substructure as a new Higgs search channel at the LHC”, *Phys. Rev. Lett.* **100** (2008) 242001, doi:10.1103/PhysRevLett.100.242001, arXiv:0802.2470.
- [20] A. J. Larkoski, S. Marzani, G. Soyez, and J. Thaler, “Soft drop”, *JHEP* **05** (2014) 146, doi:10.1007/JHEP05(2014)146, arXiv:1402.2657.
- [21] T. Sjöstrand et al., “An introduction to PYTHIA 8.2”, *Comput. Phys. Commun.* **191** (2015) 159, doi:10.1016/j.cpc.2015.01.024, arXiv:1410.3012.
- [22] CMS Collaboration, “Extraction and validation of a new set of CMS PYTHIA8 tunes from underlying-event measurements”, arXiv:1903.12179.
- [23] GEANT4 Collaboration, “GEANT4—a simulation toolkit”, *Nucl. Instrum. Meth. A* **506** (2003) 250, doi:10.1016/S0168-9002(03)01368-8.
- [24] The NNPDF collaboration et al., “Parton distributions for the lhc run ii”, *Journal of High Energy Physics* **2015** (2015), no. 4, 40, doi:10.1007/JHEP04(2015)040.

- 451 [25] NNPDF Collaboration, “Parton distributions from high-precision collider data”, *Eur.
452 Phys. J.* **C77** (2017), no. 10, 663, doi:10.1140/epjc/s10052-017-5199-5,
453 arXiv:1706.00428.
- 454 [26] J. Alwall et al., “The automated computation of tree-level and next-to-leading order
455 differential cross sections, and their matching to parton shower simulations”, *JHEP* **07**
456 (2014) 079, doi:10.1007/JHEP07(2014)079, arXiv:1405.0301.
- 457 [27] M. L. Mangano, M. Moretti, F. Piccinini, and M. Treccani, “Matching matrix elements and
458 shower evolution for top-quark production in hadronic collisions”, *JHEP* **01** (2007) 013,
459 doi:10.1088/1126-6708/2007/01/013, arXiv:hep-ph/0611129.
- 460 [28] R. Frederix and S. Frixione, “Merging meets matching in MC@NLO”, *JHEP* **12** (2012)
461 061, doi:10.1007/JHEP12(2012)061, arXiv:1209.6215.
- 462 [29] M. Czakon, P. Fiedler, and A. Mitov, “Total top-quark pair-production cross section at
463 hadron colliders through $\mathcal{O}(\alpha_s^4)$ ”, *Phys. Rev. Lett.* **110** (2013) 252004,
464 doi:10.1103/PhysRevLett.110.252004, arXiv:1303.6254.
- 465 [30] S. Alioli, P. Nason, C. Oleari, and E. Re, “NLO single-top production matched with
466 shower in POWHEG: s- and t-channel contributions”, *JHEP* **09** (2009) 111,
467 doi:10.1088/1126-6708/2009/09/111, arXiv:0907.4076. [Erratum:
468 doi:10.1007/JHEP02(2010)011].
- 469 [31] E. Re, “Single-top Wt-channel production matched with parton showers using the
470 POWHEG method”, *Eur. Phys. J. C* **71** (2011) 1547,
471 doi:10.1140/epjc/s10052-011-1547-z, arXiv:1009.2450.
- 472 [32] M. Aliev et al., “HATHOR: HAdronic Top and Heavy quarks crOss section calculator”,
473 *Comput. Phys. Commun.* **182** (2011) 1034, doi:10.1016/j.cpc.2010.12.040,
474 arXiv:1007.1327.
- 475 [33] P. Kant et al., “HATHOR for single top-quark production: Updated predictions and
476 uncertainty estimates for single top-quark production in hadronic collisions”, *Comput.
477 Phys. Commun.* **191** (2015) 74, doi:10.1016/j.cpc.2015.02.001,
478 arXiv:1406.4403.
- 479 [34] T. Gehrmann et al., “ W^+W^- production at hadron colliders in next to next to leading
480 order QCD”, *Phys. Rev. Lett.* **113** (2014) 212001,
481 doi:10.1103/PhysRevLett.113.212001, arXiv:1408.5243.
- 482 [35] J. M. Campbell and R. K. Ellis, “An update on vector boson pair production at hadron
483 colliders”, *Phys. Rev. D* **60** (1999) 113006, doi:10.1103/PhysRevD.60.113006,
484 arXiv:hep-ph/9905386.
- 485 [36] LHC Dark Matter Working Group, “Recommendations of the LHC dark matter working
486 group: Comparing LHC searches for dark matter mediators in visible and invisible decay
487 channels and calculations of the thermal relic density”, *Phys. Dark Univ.* **26** (2019)
488 100377, doi:10.1016/j.dark.2019.100377, arXiv:1703.05703.
- 489 [37] CMS Collaboration, “Identification of heavy, energetic, hadronically decaying particles
490 using machine-learning techniques”, *JINST* **15** (2020), no. 06, P06005,
491 doi:10.1088/1748-0221/15/06/P06005, arXiv:2004.08262.

- [492] [38] CMS Collaboration, “Electron and photon reconstruction and identification with the
[493] CMS experiment at the CERN LHC”, *JINST* **16** (2021) P05014,
[494] doi:10.1088/1748-0221/16/05/P05014, arXiv:2012.06888.
- [495] [39] CMS Collaboration, “Performance of the CMS muon detector and muon reconstruction
[496] with proton-proton collisions at $\sqrt{s} = 13$ TeV”, *JINST* **13** (2018) P06015,
[497] doi:10.1088/1748-0221/13/06/P06015, arXiv:1804.04528.
- [498] [40] C. Collaboration, “Identification of hadronic tau lepton decays using a deep neural
[499] network”, *JINST* **17** (2022) P07023, doi:10.1088/1748-0221/17/07/P07023,
[500] arXiv:2201.08458.
- [501] [41] E. Bols et al., “Jet Flavour Classification Using DeepJet”, *JINST* **15** (2020), no. 12, P12012,
[502] doi:10.1088/1748-0221/15/12/P12012, arXiv:2008.10519.
- [503] [42] J. M. Lindert et al., “Precise predictions for V+jets dark matter backgrounds”, *Eur. Phys.
[504] J. C* **77** (2017) 829, doi:10.1140/epjc/s10052-017-5389-1, arXiv:1705.04664.
- [505] [43] CMS Collaboration, “Performance of the CMS missing transverse momentum
[506] reconstruction in pp data at $\sqrt{s} = 8$ TeV”, *JINST* **10** (2015) P02006,
[507] doi:10.1088/1748-0221/10/02/P02006, arXiv:1411.0511.
- [508] [44] CMS Collaboration, “Search for new physics in final states with an energetic jet or a
[509] hadronically decaying W or Z boson and transverse momentum imbalance at
[510] $\sqrt{s} = 13$ TeV”, *Phys. Rev. D* **97** (2018) 092005, doi:10.1103/PhysRevD.97.092005,
[511] arXiv:1712.02345.
- [512] [45] J. Conway, “Incorporating Nuisance Parameters in Likelihoods for Multisource Spectra”,
[513] doi:10.5170/CERN-2011-006.115, arXiv:1103.0354. Comments: Presented at
[514] PHYSTAT 2011, CERN, Geneva, Switzerland, January 2011, to be published in a CERN
[515] Yellow Report.
- [516] [46] A. L. Read, “Presentation of search results: The CL_s technique”, *J. Phys. G* **28** (2002) 2693,
[517] doi:10.1088/0954-3899/28/10/313.
- [518] [47] T. Junk, “Confidence level computation for combining searches with small statistics”,
[519] *Nucl. Instrum. Meth. A* **434** (1999) 435, doi:10.1016/S0168-9002(99)00498-2,
[520] arXiv:hep-ex/9902006.
- [521] [48] G. Cowan, K. Cranmer, E. Gross, and O. Vitells, “Asymptotic formulae for
[522] likelihood-based tests of new physics”, *Eur. Phys. J. C* **71** (2011) 1554,
[523] doi:10.1140/epjc/s10052-011-1554-0, arXiv:1007.1727. [Erratum:
[524] doi:10.1140/epjc/s10052-013-2501-z].
- [525] [49] G. Busoni et al., “Recommendations on presenting LHC searches for missing transverse
[526] energy signals using simplified s-channel models of dark matter”, *Phys. Dark Univ.* **27**
[527] (2020) 100365, doi:10.1016/j.dark.2019.100365, arXiv:1603.04156.